Modified cellular automaton model for the prediction of dendritic growth with melt convection

M. F. Zhu,[1,*] S. Y. Lee,[2] and C. P. Hong[2]

[1]*Department of Materials Science and Engineering, Southeast University, Nanjing 210096, China*
[2]*Center for Computer-Aided Materials Processing (CAMP), Department of Metallurgical Engineering, Yonsei University,*
Shinchon-dong 134, Seodaemun-ku, Seoul 120-749, Korea

A modified cellular automaton (MCA) coupled with a momentum and species transport model has been developed in order to predict the evolution of dendritic morphology during solidification of alloys in the presence of melt convection. In the present model, the cellular automaton algorithm for dendritic growth is incorporated with the transport model, for calculating fluid flow and mass transfer by both convention and diffusion. The MCA model takes into account the effects of the constitutional undercooling and the curvature undercooling on the equilibrium interface temperature. It also considers the preferred growth orientation of crystals and solute redistribution during solidification. In the transport model, which is coupled with cellular automaton approach, the SIMPLE scheme is employed to solve the governing equations of momentum and species transfers. The present model was applied to model solutal dendritic growth of an Al-3mass%Cu alloy in a forced flow. The simulations reproduced the typical asymmetric growth features of convective dendrites with various preferred orientations. The effects of inlet flow velocity on the solute redistribution and the growth velocity of a dendritic tip were quantitatively investigated.

I. INTRODUCTION

Dendritic structures are commonly observed in casting and welding of many metals and alloys. The details of dendritic morphology are directly related to mechanical properties of final products. Dendritic growth is also regarded as a well-studied example of pattern formation in nonequilibrium physics, where a complex pattern evolves from simple starting conditions [1,2]. Thus, the mechanism of dendritic microstructure formation has been of great interest for both academic research and practical application [3,4].

Evolution of dendritic microstructures is a complicated physical process controlled by the interplay of thermal, solutal, capillary, and kinetic length or time scale [5,6]. Particularly, some degree of fluid motion is nearly always present in most solidification processes, whether by buoyant natural convection or forced convection [7–9]. Experimental observations and theoretical analyses show that fluid flow has a profound effect on the morphology of the solid-liquid interface and often dominates the phase transition. Convective heat and mass transfers perturb significantly concentration and temperature distributions, which alters the pattern formation of microstructures [7,10,11].

Many theoretical and experimental efforts have so far been devoted to characterize dendritic growth behavior in the presence of convection [4,8,11–24]. Experiments on the dendritic growth of transparent organic materials from supercooled melts under normal or microgravity reveal small discrepancies from the classic Ivantsov relation between Peclet number and dimensionless supercooling. Under terrestrial gravity and low supercooling conditions, dendritic growth is dominated by convection [2,25,26]. However, quantitative experimental investigations of flow effects on the dendrite tip selection have yielded inconsistent results [11,12,18]. On the

other hand, the presence of melt convection considerably complicates the theoretical analysis of free dendritic growth in metals and alloys, which needs a nonlinear coupling between fluid flow, transport of heat and species, and the solidification process. Analytical solutions for dendritic growth in the presence of fluid flow are thus limited to simple situations and the rigorous treatments have still remained lacking [5,21,22,24,27,28]. Consequently, the effect of convection on the dendritic growth during solidification has not yet been fully understood [16].

Significant progress in numerical modeling has recently been made with the advent of powerful computers and advanced numerical techniques. It plays an increasing role in the studies of microstructural evolution during solidification. Regarding the situation of dendritic growth in the presence of melt convection, in order to better understand the underlying physics in this process, description and visualization of transport phenomena and a complete time-dependent interaction of fluid flow with phase transition become crucial. For this purpose, numerical studies are highly desired to provide satisfactory information on the fluid mechanics, heat and mass transfer in melt, as well as microstructure evolution undergoing solidification.

Several studies on the coupling mechanisms between the solidification process and melt convection have recently been carried out by phase-field models [3,5–7,9,10,29–38] and other numerical techniques, such as the sharp-interface method [39], the front tracking method [27,40], and the lattice Boltzmann model [41,42]. The simulations could reproduce asymmetrical dendritic growth features, such as the deflection behavior of dendritic growth, the tip growth velocity, and the side-branching enhanced in the upstream direction, but largely hindered in the downstream direction. Using a two-dimensional phase-field model incorporated with the solution of Navier-Stokes equation and thermal noise, Tong [3,5,9], and Beckermann *et al.* [6,32] simulated the free thermal dendritic growth of a pure substance under high super-

*Electronic address: zhumf@seu.edu.cn

coolings with melt convection. The tip-operating state and the side-branching development of dendrite were investigated as a function of flow rate, growth orientation with respect to the flow direction, as well as anisotropy strength. Their results agree well with the Oseen-Ivantsov solution if the tip radius based on a parabolic fitting is estimated [5].

Lan *et al.* [29–31] carried out the phase-field simulations based on an adaptive finite volume method. Since a large domain (over 218 in the ratio of cell size), while keeping very small cell size at the interface, was available, they could simulate the dendrites to evolve secondary arms even at low undercoolings with melt flow.

Tönhardt and Amberg [7,33,34] studied the effects of natural and forced convection on the growth of pure succinoinitrile (SCN) by a phase-field model on an adaptive finite element mesh. They found that different initial preferred growth orientation of a nucleus gives different vertical growth velocities. The results depend also on flow strength, undercooling, and the degree of anisotropy. Using a similar approach, Jeong *et al.* [35,37,38] investigated the effects of fluid flow on two-dimensional (2D) and (3D) dendritic growth. They compared the simulation results with the available theories and experiments, and concluded that there are significant open questions remaining about the evolution of microstructure when flow is present [37].

All the above numerical activities have focused on the free dendritic growth with convection in pure materials, where the driving force is purely thermal undercooling. Shin and Hong [43] developed a modified cellular automaton model with a diffuse interface to study the effect of convection on dendritic growth morphology of Al-Cu alloys. This model is based on the coupling of a cellular automaton algorithm for dendritic growth and a continuum diffuse interface model as known from the phase-field methodology, for solving the species and momentum transfers with convection. This model was applied to investigate the asymmetrical growth behavior of primary dendrite arms under various conditions, such as the preferred orientation of a crystal, the inlet flow velocity, the initial liquid concentration, and the initial undercooling of melt.

During recent years, modified cellular automaton (MCA) models have emerged as a powerful computational tool and achieved considerable importance in modeling complex evolving interfacial patterns and a range of phase transitions during solidification. They can successfully predict the evolution of dendritic growth features, including the growth and coarsening of primary trunks, the branching of secondary and tertiary dendrite arms, as well as the solute redistribution [44–49]. A MCA model developed by the authors has also been extended into multiphase systems to model the microstructure formation in regular and irregular eutectic and peritectic alloys [50–52].

The purpose of the present study is to extend a two-dimensional MCA model into the solidification system including melt convection. It involves the simultaneous numerical solution of the fully coupled cellular automaton growth algorithm together with the momentum and species conservation equations in liquid, solid, and solid/liquid interface. The present model was applied to predict the solutal
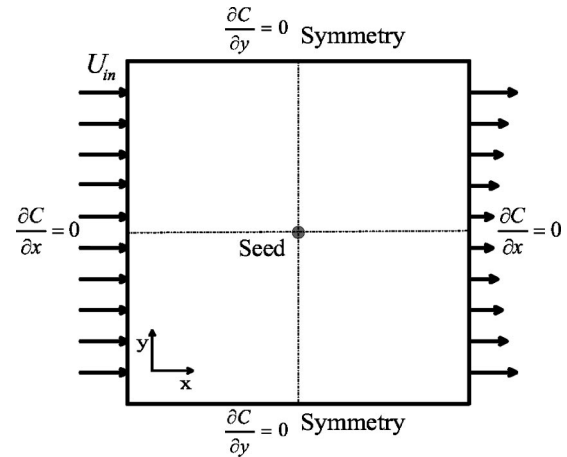

FIG. 1. Illustration of the physical system used in the simulation of dendritic growth with melt convection.

dendritic growth of an Al-3mass%Cu alloy in a forced flow. A quantitative study of the effect of melt convection on the solute redistribution and dendritic growth dynamics is presented.

II. MODEL DESCRIPTION AND MATHEMATICAL FORMULATION

A. Model description

In order to predict the dendritic microstructures solidified in a flowing melt, the MCA model for dendritic growth is coupled with a transport model for calculating solute transfer by both convection and diffusion during solidification. Figure 1 illustrates the physical system used in the present study. The two-dimensional computational domain is divided into a uniform orthogonal arrangement of cells. Each cell is characterized by several variables, such as temperature, concentration, crystallographic orientation, solid fraction, flow vector, pressure vector, etc., and marked as the state of liquid, solid, or interface. Since the emphasis of the present study is on the solutally driven dendritic growth with a forced flow, for the sake of simplicity, the temperature field inside the domain is considered as uniform and with a constant thermal undercooling. The undercooled melt, assumed as an incompressible Newtonian fluid, enters through the left boundary of the domain with a uniform inlet flow velocity denoted as U_{in} and flows past the solidified cells in the center, and then exits from the right boundary of the domain. The top and bottom surfaces of the domain are treated as the symmetrical boundaries for fluid flow. The zero-flux boundary condition is imposed for mass transfer at four surfaces of the domain. The solidified dendrite is assumed to be rigid and stationary. No slip boundary condition is applied at the solid-liquid interface. The cellular automaton evolves in discrete time step, and the state of a cell at a particular time is calculated from the local rule. As the dendrite grows into the undercooled and flowing melt, the geometry of the solid/liquid boundary changes, which in turn triggers an increasing complex fluid flow. The governing equations and numerical algorithms for calculating flow field, solute field, and dendritic growth are described in detail below.

B. Cellular automaton growth

As elucidated in the present author's previous papers [45–48], in MCA models three contributions (thermal, solutal, and curvature effects) are generally taken into account in the modeling of microstructure evolution, and the total undercooling at a dendritic tip is thus given by

$$\Delta T = \Delta T_T + \Delta T_C + \Delta T_R, \tag{1}$$

where ΔT_T, ΔT_C, and ΔT_R are the undercooling contributions associated with the thermal, the solutal, and the curvature effects, respectively. In the present study, the thermal undercooling ΔT_T is assumed constant, while the solutal and the curvature undercoolings are dependent on the local concentration $C(t_n)$ and the mean curvature $\bar{K}(t_n)$ at the solid/liquid interface. Both $C(t_n)$ and $\bar{K}(t_n)$ will vary as a dendrite evolves. Therefore, the local undercooling at the solid/liquid interface at time t_n, $\Delta T(t_n)$, can be calculated by

$$\Delta T(t_n) = \Delta T_T + m[C(t_n) - C_0] - \Gamma \bar{K}(t_n), \tag{2}$$

where m is the liquidus slope, C_0 is the initial composition, and Γ is the Gibbs-Thomson coefficient. The interface mean curvature $\bar{K}(t_n)$ in Eq. (2) is calculated using the same manner as in the literature [43], which introduced some concepts of phase-field methods to evaluate the average interface curvature and thus reduced the cell size dependency.

The classical sharp-interface model [6,53,54] is employed to relate the normal interface growth velocity V_n to the interface undercooling by

$$V_N = \mu_k \Delta T(t_n), \tag{3}$$

where μ_k is the interface kinetics coefficient.

It is well known that dendrites always grow in specific crystallographic orientations and the selection of the dendrite growth direction is determined by the anisotropy properties of the interface [55]. Particularly, the theoretical analysis and experimental evidences have shown that anisotropic kinetics might play a crucial role in the stability mechanisms, the selection of dendrite tip's velocity and the development of solidification microstructures [55,56]. Therefore, as described in the previous paper [43], the present model accounts for the anisotropy in both interfacial kinetics and thermodynamics. Similar to that used in the literature [27,57–59], the crystal growth velocity V_g is assumed as

$$V_g = V_N \{1 + \delta_k \cos[4(\theta - \theta_0)]\}, \tag{4}$$

where δ_k is the degree of the kinetic anisotropy, θ is the angle between the normal of the solid/liquid interface and the horizontal direction, and θ_0 is the preferred growth orientation of a crystal. The angle θ is obtained from the gradient of solid fraction at the solid/liquid interface according to

$$\theta = \arctan\left(\frac{\partial f_s}{\partial y} \middle/ \frac{\partial f_s}{\partial x}\right). \tag{5}$$

Using the thermodynamic anisotropy δ_t related to the crystal orientation, Gibbs-Thomson coefficient Γ is evaluated as follows:

$$\Gamma = \bar{\Gamma}\{1 - \delta_t \cos[4(\theta - \theta_0)]\}, \tag{6}$$

where $\bar{\Gamma}$ indicates the average Gibbs-Thomson coefficient.

C. Momentum and species transfers

Considering that the solute redistribution is affected by fluid flow, the continuity and Navier-Stokes equations for incompressible fluid flow are written as follows.

Equation of continuity is

$$\vec{\nabla} \cdot (\vec{u}) = 0. \tag{7}$$

Navier-Stokes equation is

$$\rho \frac{\partial(\vec{u})}{\partial t} + \rho(\vec{u}) \cdot \vec{\nabla}(\vec{u}) = -\vec{\nabla}P + \vec{\nabla} \cdot [\mu \vec{\nabla}(\vec{u})], \tag{8}$$

where $\vec{u}$ is the velocity vector, ρ is the density which is considered to be identical and constant in liquid and solid phases, μ is the viscosity, and P is the hydrostatic pressure.

It is assumed that the concentrations of solid and liquid at the solid/liquid interface are in equilibrium. When solidification at the solid/liquid interface occurs, the solute partition between liquid and solid is given by

$$C_s^* = kC_l^*, \tag{9}$$

where k is the partition coefficient, C_s^* and C_l^* are the interface equilibrium concentrations in solid and liquid phases, respectively. The governing equation for solute redistribution by both convention and diffusion in the whole domain is given by

$$\frac{\partial C}{\partial t} + (\xi \vec{u}) \cdot \vec{\nabla} C = D\nabla^2 C + C(1-k)\frac{\partial f_s}{\partial t}, \tag{10}$$

where D is the solute diffusion coefficient. The second term on the right-hand side of Eq. (10) indicates the amount of solute rejected or absorbed at the solid/liquid interface, resulting from the generation of solid fraction. ξ is a parameter which is dependent on the state of a cell: $\xi=1$ $(f_s<1)$ and $\xi=0$ $(f_s=1)$. The species transfer in solid is purely controlled by diffusion $(\xi=0)$.

III. NUMERICAL ALGORITHM

A. Cellular automaton for simulating dendritic growth

In the present study, the calculation domain was divided into 201×201 uniform and square cells with a cell size of 0.4 μm. Eight neighbor cells, which include the four nearest neighbor cells and the four second-nearest neighbor cells, were taken into consideration to determine the interface

cells. Each cell in the whole domain was given an index indicating the cell state as solid ($f_s = 1$), liquid ($f_s = 0$), and interface ($0 \leqslant f_s < 1$). The interface cell also should satisfy the condition that at least one of its eight neighbors is solid. At the beginning of simulation, a solid seed consisting of one cell, having a preferred growth orientation of θ_0 and the concentration of kC_0, was located in the center of the domain. Other cells were filled with liquid having a uniform initial composition. The growth of the solid seed was initiated by an imposed thermal undercooling $\triangle T_T$. In the present study, $\triangle T_T$ was fixed as 12 K. The growth velocities of interface cells were calculated by Eqs. (2)–(6). The change rate of solid fraction of an interface cell could thus be evaluated from the crystal growth velocity V_g as follows:

$$\frac{\partial f_s}{\partial t} = G \frac{V_g}{\triangle a}, \tag{11}$$

where t is the time, $\triangle a$ is the cell spacing and defined in a regular grid system as $\triangle a = \triangle x = \triangle y$. G is a geometrical factor related to the state of neighbor cells, which is defined by

$$G = b_0 \left(\sum_{m=1}^{4} s_m^{\mathrm{I}} + \frac{1}{\sqrt{2}} \sum_{m=1}^{4} s_m^{\mathrm{II}} \right), \tag{12}$$

where b_0 is an empirical coefficient and chosen as 0.4 in the present simulation. s^{I} and s^{II} indicate the states of the nearest neighbor cells and the second-nearest neighbor cells, respectively. According to the state of a neighbor cell, s^{I} and s^{II} are determined by

$$s^{\mathrm{I}}, s^{\mathrm{II}} = \begin{cases} 0 & (f_s < 1) \\ 1 & (f_s = 1). \end{cases} \tag{13}$$

The geometrical factor defined by Eqs. (12) and (13) is used to account for the fact that as the number of solid neighbor cells increases, the solidification rate of a cell increases. Equation (12) also reflects the consideration that the geometrical relation between cells is proportional to the cell spacing, i.e., the effect of the second-nearest neighbor cells is weaker than that of the nearest neighbors.

According to Eq. (11), at one time step, the solid fraction increment of an interface cell labeled as i can be calculated by

$$\triangle f_s^i = G^i \frac{V_g^i}{\triangle a} \triangle t. \tag{14}$$

Therefore, the solid fraction of this interface cell at time t_n is given by

$$f_s^i(t_n) = \sum_{n=1}^{N} G^i(t_n) \frac{V_g^i(t_n)}{\triangle a} \triangle t_n, \tag{15}$$

where N indicates the iteration number. When $f_s^i(t_n) = 1$, the cell i transforms its state from interface to solid. This newly solidified cell in turn captures a set of its liquid neighbors to be the new interface cells. The solidification will thus go on in the next time step.

By means of the algorithm described above, the primary dendrite will grow and coarsen with the preferential growth orientation. As crystal growth proceeds, a certain amount of solute is rejected by the solidified cells and accumulates in front of the solid/liquid interface. According to Eq. (2), the resulting local solute enrichment at the interface gives rise to the uneven local undercoolings and thus destabilizes the interface stability, leading to the side branching into the secondary arms.

B. Solution scheme for momentum and species transfers

In order to calculate the incompressible flows around the dendrite as well as the solute redistribution by both convention and diffusion during solidification, a fully coupled solving scheme for momentum and species transfers was adopted. The continuity and the momentum equations, Eqs. (7) and (8), were solved by the SIMPLE algorithm [60] based on the staggered grids. An implicit control volume based finite difference method, using the tridiagonal matrix algorithm, was employed for solving the time-dependent terms of Navier-Stokes equation, Eq. (8), and the species conservation equation, Eq. (10). Both convection and diffusion terms were evaluated by the hybrid scheme. Since the system includes liquid, solid, and interface, the diffusion coefficient D in Eq. (10) is taken as D_l and D_s in liquid and solid, respectively. In order to satisfy the suitable jump conditions across the phase boundary, the solute diffusion coefficient at the interface region is evaluated as follows.

At the interface cell,

$$D = D_{int} = f_s D_s + (1 - f_s) D_l, \tag{16}$$

and at the liquid/interface boundary,

$$D = D_{l/int} = \frac{2 D_l D_{int}}{D_l + D_{int}}. \tag{17}$$

The solute diffusion coefficient at the solid/interface boundary, $D_{s/int}$, can also be given in a similar form of $D_{l/int}$ as shown in Eq. (17). The boundary conditions for momentum and species transfers on the surfaces of the calculation domain have been described in Sec. II A.

C. Coupling of the MCA with the transport models

At a time step interval, the simulation of momentum and species transfers provides a transient solute distribution in the domain, based on which, the local undercoolings and the growth velocities of the interface cells are calculated using Eqs. (2)–(6). The solid fraction increment $\triangle f_s$ of the interface cells can thus be calculated by Eq. (14). According to Eq. (9), the solid fraction increment $\triangle f_s$ will liberate the amount of solute, $\triangle C = \triangle f_s (C_l^* - C_s^*)$, which is added to the remaining liquid in the same cell and its surrounding neighbor cells. Thus, the overall solute in the domain can be kept constant. At the end of this time step, all the cells in the domain are scanned to check the solid fraction of each cell. The distribution of flow velocity is then updated by the state parameter ξ according to the new solid fraction profile. It is obvious that the newly solidified cells become new obstacles in the next step of the iterative calculation of fluid flow. Using these updated velocity and solute profiles, the calculations of fluid flow and species transfer can be continued.

TABLE I. Physical properties used in the present simulation [6,43,45].

Symbol	Definition and units	Value
T_f^0	Melting temperature of pure Al (K)	933.6
k	Partition coefficient	0.17
m_l	Liquidus slope (K/mass%)	-3.36
D_l	Solute diffusion coefficient in liquid (m^2/s)	3.0×10^{-9}
D_s	Solute diffusion coefficient in solid (m^2/s)	3.0×10^{-13}
μ_k	Interface kinetics coefficient (m/s K)	0.002
δ_k	Kinetic anisotropy strength	0.3
$\bar{\Gamma}$	Average Gibbs-Thomson coefficient (mK)	1.7×10^{-7}
μ	Viscosity (P)	0.014
ρ	Density (kg/m^3)	2.475×10^3

This series of calculations is repeated until the end of simulation.

As explained previously, momentum and species transfers are implicitly calculated, whereas the dendritic growth is simulated by an explicit scheme. The largest time step for iteration is thus limited by the maximum change rate of solid fraction. In order to avoid numerical instability, it is considered that at least five time intervals are needed to complete the solidification of an interface cell so that the stable time step for the simulation is determined by

$$\triangle t = \frac{1}{5} \left(\frac{\partial f_s}{\partial t} \right)^{-1}_{max}, \quad (18)$$

where $(\partial f_s / \partial t)_{max}$ is the maximum change rate of solid fraction obtained by scanning all interface cells during one time step.

The physical parameters used in the present simulation are listed in Table I. In order to quantitatively study the dendritic growth velocity as a function of various controlled parameters, the time and the tip growth velocity were scaled with $\tau_0 = w_0^2/(\mu_k \Gamma)$, and w_0/τ_0, respectively, where w_0 is the reference length and it was chosen as 10^{-5} m.

IV. RESULTS AND DISCUSSION

A. The asymmetrical dendritic growth behavior in a forced flow

In order to examine the influence of grid anisotropy on dendritic growth, we first performed the simulation of free dendritic growth without melt convection. Figure 2 shows the simulated dendritic morphologies and solute profiles of an Al-3mass%Cu alloy solidified from a static undercooled melt ($\triangle T = 12$ K) with three different preferred growth orientations of (a) 0°, (b) 30°, and (c) 45° with respect to the horizontal direction. It can be seen from Fig. 2 that the present model can successfully generate the dendrite shapes with different crystallographic orientations. Particularly, the nearly exact symmetric dendrite shapes and solute distribution patterns can be obtained in the cases of 0° and 45° orientations. Indeed, the dendrite with the orientation of 30° shows some asymmetrical side branching which might be caused by the CA mesh anisotropy. In addition, the mesh
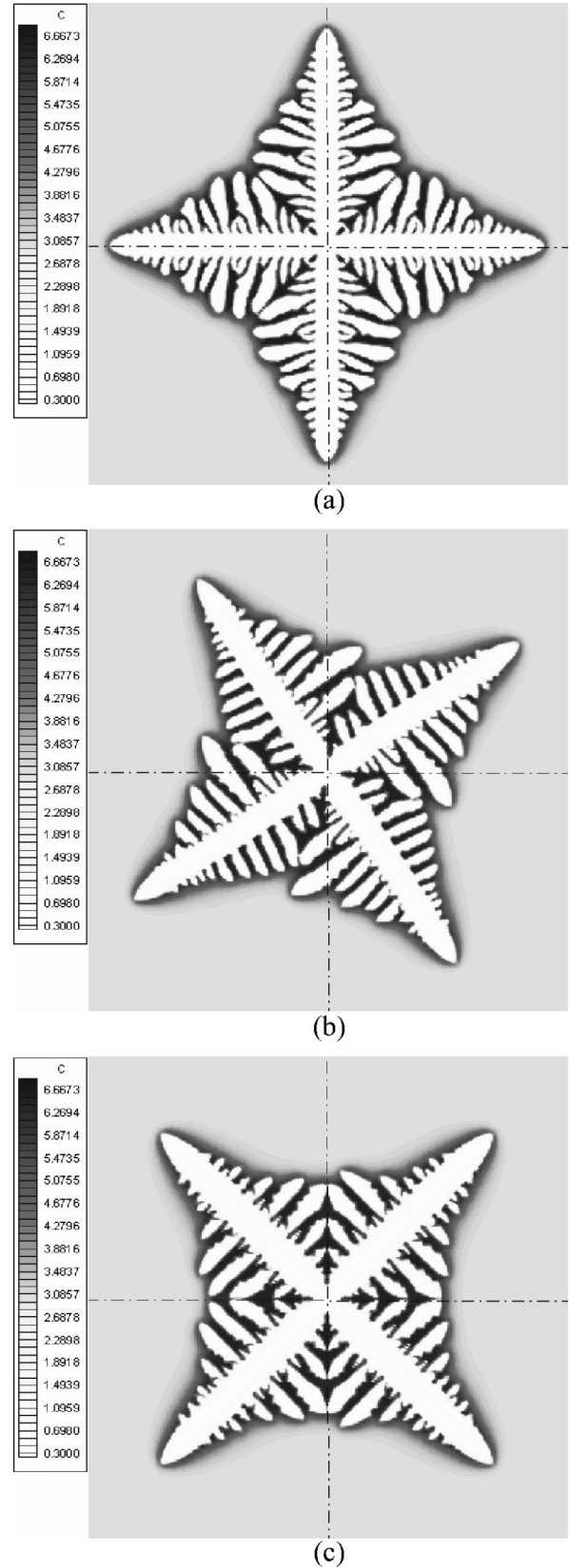

FIG. 2. Simulated dendrite morphologies and solute profiles of an Al-3mass%Cu solidified in a static melt with various preferred growth orientations: (a) $\theta_0 = 0°$, (b) $\theta_0 = 30°$, and (c) $\theta_0 = 45°$ ($f_s = 0.2$).

anisotropy also slightly affects the tip velocity of dendrites with different orientations. The steady-state tip velocities measured from the simulations of Figs. 2(a), 2(b), and 2(c) are 0.125, 0.130, and 0.127, in the unit of w_0/τ_0, corresponding to 0°, 30°, and 45°, respectively. The differences among them are less than 4%. Some researchers have also carried out grid anisotropy test using phase-field models. The results of Lan *et al.* [29] show that the dendrite tip grows slightly faster for 30° and 45° orientations with a less than 3% difference. Beckermann *et al.* [6] found that the steady-state tip velocity at 45° is 4.7% lower than the base case. Besides, as clarified in our previous paper [52], the present CA approach also has the limitation of grid size dependency. Efforts will be continuously devoted to further improve the CA growth algorithm for reducing the grid anisotropy and the grid size dependency of simulations.

Figure 3 represents the simulated dendritic morphologies, solute profiles, and flow fields of the free dendritic growth in a forced flow with an inlet flow velocity of $U_{in}=0.03$ m/s. Other conditions are identical to those of Fig. 2. The velocity vector plots in Fig. 3 indicate the real strength and the direction of flow. For a clearer visualization, the flow field is represented by ten times coarser than the available computational nodes, i.e., every 10×10 cells show one flow vector. Comparing Fig. 3 with Fig. 2, it can be noted that the dendrite shapes and solute fields are significantly influenced by fluid flow. For three different orientations, the growth of the dendrite arms and side branching are all promoted on the upstream side and inhibited on the downstream side. As the dendrite grows, solute atoms are rejected in the liquid ahead of the solid/liquid interface, which are washed away from the upstream to the downstream direction by fluid flow, resulting in the asymmetrical solute profile in liquid, i.e., the concentration in the left region is lower than that in the right. According to Eq. (2), under a uniform temperature field, the lower the concentration, the larger the local undercooling. Therefore, the dendrite growth velocity in the upstream direction region is faster than that in the downstream region, resulting in an asymmetrical dendritic growth morphology. Moreover, the primary arms and the side branches in the upstream direction are obviously coarser than those in the downstream direction. It is understandable that convection promotes removing solute from solid/liquid interface in the upstream side and thus increases the interface stabilities, resulting in relative coarsening dendritic morphology. This phenomenon is also considered to fundamentally coincide with the experimental observations of Trivedi *et al.* [8].

Figure 4 indicates that when a single dendrite grows at a 45° angle relative to the fluid flow direction, side branches appear in the upstream direction: (a) the experimental result, (b) a phase-field simulation, and (c) a MCA simulation. The experimental picture was obtained by Bouissou *et al.* [12] using a pivalic acid and ethanol alcohol (PVA-Al) system. The phase-field simulation was performed by Tong *et al.* [5] using a pure substance of SCN. The present simulation result, Fig. 4(c), was obtained from an Al-3mass%Cu alloy with a thermal undercooling of $\triangle T_T=12$ K and an inlet flow velocity of $U_{in}=0.05$ m/s. Considering that the results are from different materials and conditions, a direct quantitative
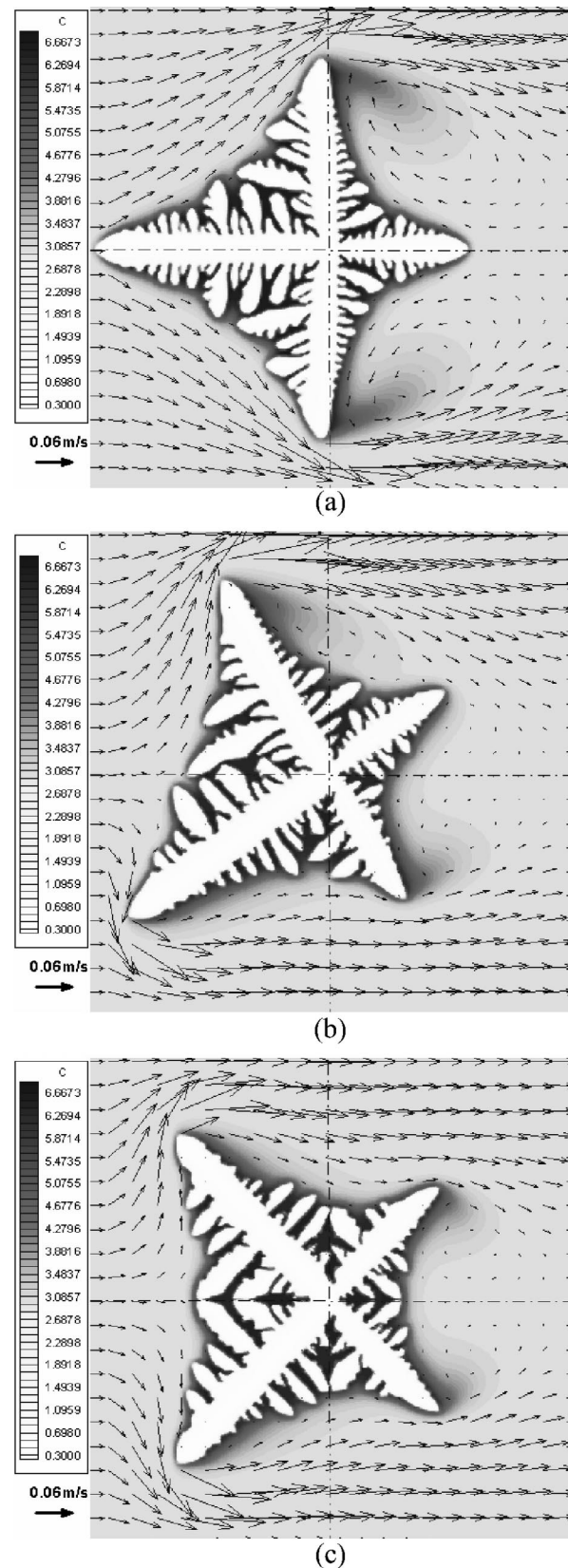

FIG. 3. Simulated dendrite morphologies, solute profiles, and velocity vectors of an Al-3mass%Cu solidified with melt convection ($U_{in}=0.03$ m/s) and various preferred growth orientations: (a) θ_0 =0°, (b) $\theta_0=30°$, and (c) $\theta_0=45°$ ($f_s=0.15$).
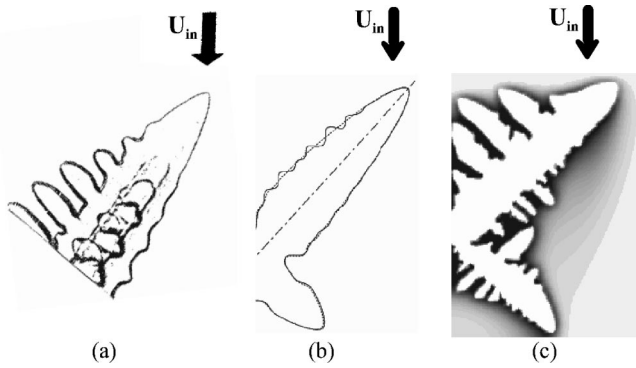
FIG. 4. Comparison of the dendrite morphologies with convection obtained by (a) experiment [12], (b) simulation of a phase-field model (solid line, with noise; dot line, without noise) [5], and (c) simulation of the present work.

comparison among them may be difficult to make. Nevertheless, they apparently exhibit a typical feature of the asymmetric dendritic growth behavior in a forced convection: primary arms and side branches are preferentially developed in the upstream direction and largely suppressed in the downstream direction. It is noted that in case of a phase-field simulation, if no artificial noise is introduced, there are few differences between the upper side and the lower side of the main stem. Both sides present the needle crystal morphology without side branches as indicated by the dotted line in Fig. 4(b). However, according to the MCA simulation, the asymmetrical growth and side-branching features for a convective dendrite can be naturally predicted as shown in Fig. 4(c).

In order to investigate the effect of flow on dendritic growth, the time histories of solid fraction, tip concentration, and tip velocity for the case of Fig. 3(a) are measured and shown in Figs. 5 and 6. The data of the dendritic growth in the absence of convection are also plotted in the figures for comparison. In Fig. 5, the solid fraction is measured from the half domains of the upstream and the downstream regions, respectively. It can be seen from Fig. 5 that the increase rate of solid fraction in the upstream region is faster, while the one of the downstream region is slower than the case of without flow. When the growth time is $t/\tau_0 = 125$, the solid fractions in the upstream and the downstream regions are about 112% higher and 21% lower than the value in the
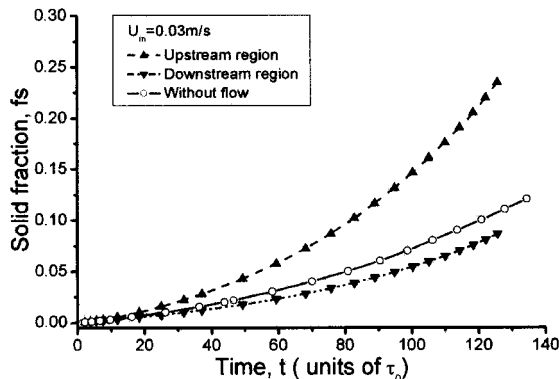

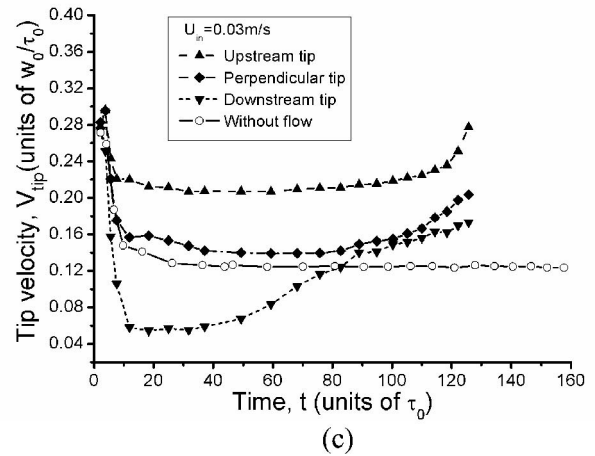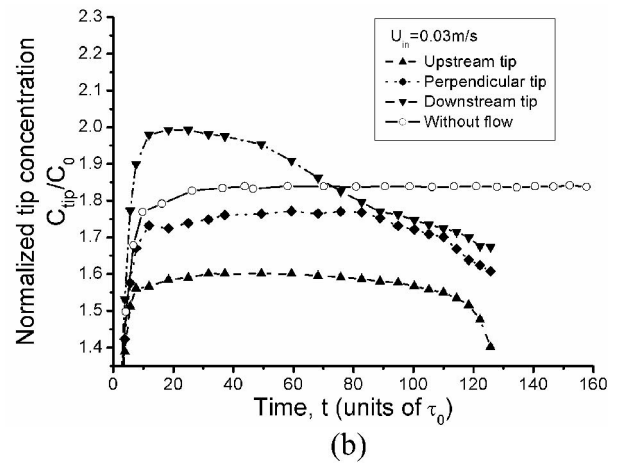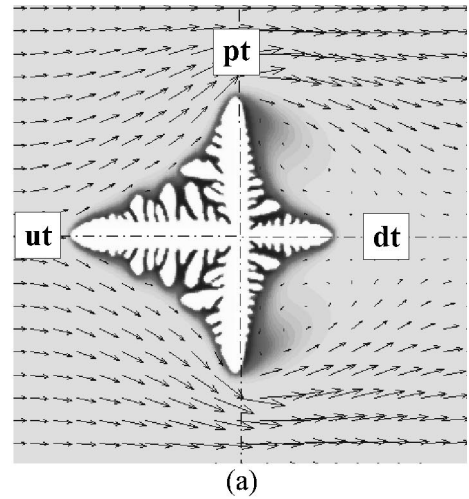FIG. 5. Solid fraction vs time under the condition of $U_{in} = 0.03$ m/s and $\theta_0 = 0°$.

FIG. 6. Time histories of the tip concentration and the tip velocity under the condition of $U_{in} = 0.03$ m/s and $\theta_0 = 0°$: (a) a schematic drawing of a dendrite, (b) tip concentration vs time, and (c) tip velocity vs time.

absence of flow, respectively. In addition, it can be noted that at $t/\tau_0 = 125$, the total solid fraction is about 0.16 with flow, but 0.11 without flow. This indicates that convection accelerates the average solidification rate. Because forced convection is more efficient than diffusion to transport the

rejected solute at the solid/liquid interface into the far field of melt, the local solute enrichment at the interface is therefore lower than the case of pure diffusion, leading to faster solidification.

Figure 6 shows the time histories of tip concentration and tip velocity for the case of Fig. 3(a). Figure 6(a) indicates the schematics of a dendrite. As shown, the tips growing to the left, the right, and the vertical directions are referred to as the upstream tip, the downstream tip, and the perpendicular tip, respectively. The tip concentration in Fig. 6(b) is normalized by the initial composition C_0. It can be seen from Fig. 6(c) that all tip velocities start from a relative large value. At the initial stage, the local undercooling for dendritic growth includes only the imposed thermal undercooling. As the solidification proceeds, the solute is liberated and enriched in the solid/liquid interface, leading to the rapid increase of concentration in front of the dendrite tips as shown in Fig. 6(b). Due to the negative liquidus slope in this alloy, the increasing local concentration at the interface will result in an increasing negative solutal undercooling and thus rapidly decreasing the tip velocity as shown in Fig. 6(c). When the growth time is about $20t/\tau_0$, the concentration ahead of the upstream tip reaches an approximately stable value. This indicates that the solute rejection is balanced by the solute transportation due to convection and diffusion. Correspondingly, the upstream tip reaches the steady-state growth with a velocity about 68% higher than that for pure diffusion. Meanwhile, the perpendicular arm tip also approaches an approximately steady-state growth and the velocity is increased by about 12% compared to the case without flow. However, in the later stage of dendritic growth, the concentrations in front of the upstream tip and the normal tip are found to decrease, leading to an increase of the tip growth velocity. This phenomenon is considered to be caused by the increasingly intense impingement of convection against the growing tips when they are close to the side boundaries.

On the contrary, the downstream arm exhibits some different growth behavior. As shown in Fig. 6(c), the growth velocity of the downstream tip quickly reaches a minimum which is $\approx 55\%$ lower than that for the case without flow, and then gradually increases until the end of the simulation. This phenomenon can be understood by observing the evolution of flow field in the vicinity of the downstream tip. Figure 7 provides an evolution sequence of dendritic growth and flow field corresponding to the conditions of Fig. 3(a) for various elapse times: (a) $37t/\tau_0$, (b) $66t/\tau_0$, and (c) $121t/\tau_0$. In order to illustrate clearly the weak flow patterns in the downstream region, the flow field of Fig. 7 is plotted using uniform vectors which only denote the flow direction but not the relative flow strength. It can be seen from Fig. 7 that at the early stage of dendritic growth, the fluid smoothly flows around the dendrite from left to right, during which it transports solute atoms from the upstream to the downstream region. The solute is mostly built up around the interface in the downstream region, resulting in a decrease of growth velocity of the downstream tip with time. As dendrite grows, the flow flux is continually enhanced. When the flow velocity is large enough, the boundary-layer separation occurs and two relatively weak clockwise vortices appear in the downstream region behind the perpendicular arms as shown in Fig. 7(b). As the clockwise rotating vortices develop, the fluid starts to flow towards the downward growing tip. The local solute is pushed away by the backflow, leading to an increase of growth velocity of the downstream tip, as shown in Fig. 7(c).

B. Effect of inlet flow velocity

A basic problem in dendrite growth is to determine the growth rate as a function of various process parameters such as the undercooling of the melt, the velocity of a controlled external flow, and the concentration of an impurity [19]. Figure 8 shows the simulated dendritic morphologies, solute profiles, and flow fields with various inlet flow velocities. The simulation of Fig. 8 was carried out for the initial composition of $C_0 = 3\,\mathrm{mass\%}\,\mathrm{Cu}$ and the preferred growth orientation of $\theta_0 = 0°$ with various inlet flow velocities of (a) 0.005 m/s, (b) 0.015 m/s, (c) 0.025 m/s, and (d) 0.05 m/s. The dendrites in Fig. 8 are all shown with a solid fraction of $f_s = 0.15$. In this figure, the flow field is also represented by uniform vectors. It can be noted that as the inlet flow velocity increases, the perpendicular tips shift more towards the incoming flow, exhibiting the deflection behavior of the dendrite arms in the upstream direction, which is consistent with the simulation results of the literature [27,34,42]. Meanwhile, the upstream and perpendicular tips become thicker. The branches of the perpendicular stem on the upstream side are also found to be increasingly coarsening. Particularly, as shown in Fig. 8(d), when $U_{in} = 0.05$ m/s, one secondary arm outgrows from its neighboring branches whereas the growth of the neighbors is largely prohibited. It is evident that once one or more relative larger side branches are developed by competitive growth, the small neighboring branches will be sheltered from the flow by the outgrown secondary arms. The solute, rejected by the growing long branches or pushed by the oncoming flow, will be heavily packed at the boundary layer ahead of these small branches and they are thus hindered from further growing. Accordingly, convection will promote competitive growth and coarsening of the secondary dendrite arms. However, this trend is found not exactly true for the side branches of the upstream stem. It seems that the effect of convection on the side branching and coarsening is also related to the flow direction with respect to the preferred growth orientation of the side branches.

On the other hand, as the inlet flow velocity increases from 0.005 m/s to 0.015 m/s, the downstream tip and the side branches behind the perpendicular tips are more prohibited from growing, as shown in Figs. 8(a) and 8(b). However, when U_{in} increases to 0.025 m/s, the downstream stem becomes a little longer and thicker compared to the case of $U_{in} = 0.015$ m/s. This is due to the fact that two clockwise rotating vortices appear behind the perpendicular arms, which perturb the solute pattern on the downstream region as shown in Fig. 8(c). When the inlet flow velocity increases further to 0.05 m/s, the clockwise rotating vortices become larger and stronger, promoting the growth of the downstream tip and resulting in a little longer and thicker downstream arm, as shown in Fig. 8(d).
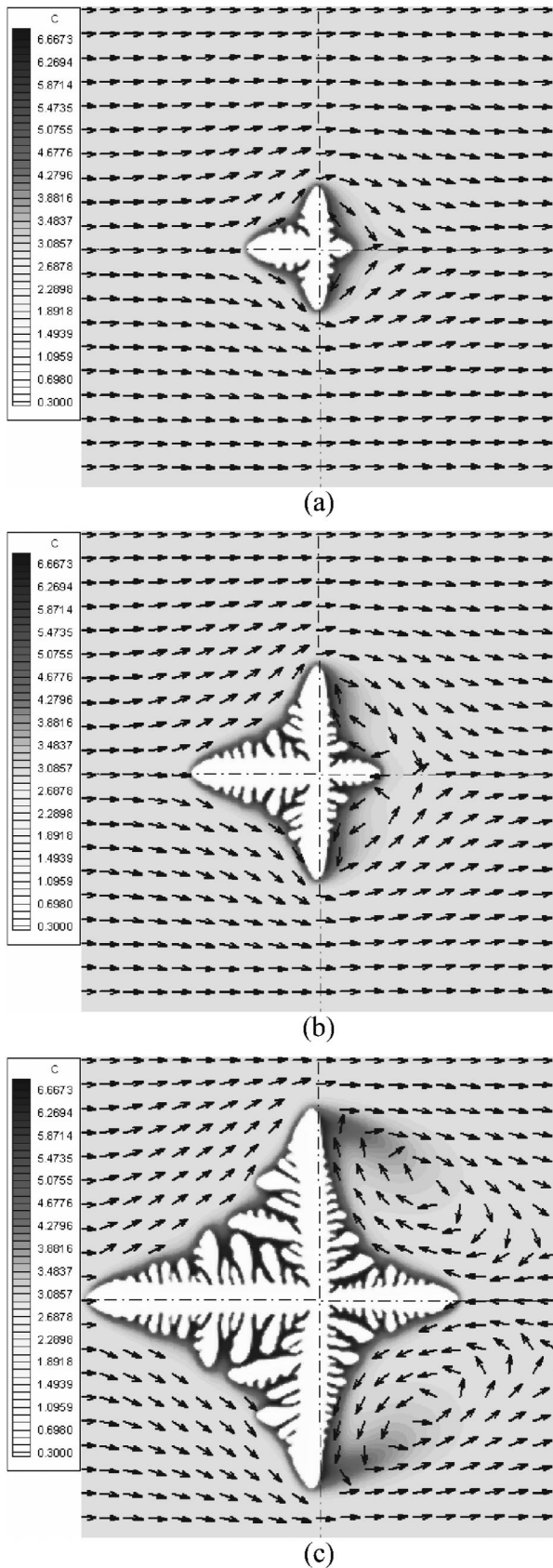
(a)

(b)

(c)

FIG. 7. Evolution of dendrite morphology and flow field under the condition of $U_{in}=0.03$ m/s and $\theta_0=0°$ with various elapse times: (a) $t/\tau_0=37$, (b) $t/\tau_0=66$, and (c) $t/\tau_0=121$.

Figures 9 and 10 indicate the normalized tip concentration and the tip growth velocity obtained from the simulations of Fig. 8. The data in the absence of flow are also included in the figures for comparison. As shown in Fig. 9, fluid flow causes a decrease in the concentration around the dendrite tips of both the upstream and the perpendicular arms. With an increase of the inlet velocity, the effect of flow on the tip concentration is enhanced. This is consistent with the experimental observations which show that as the convection becomes stronger, the tip composition decreases [8]. In addition, it is to be noted that the effect of convection is more significant for the upstream tip. As discussed previously, in the later stage, the tip concentration decreases further due to the vigorous impingement of convection with the growing tip. However, for the case of $U_{in}=0.005$ m/s, the tip concentration almost holds the steady state value till the end of simulation because of the weak incoming flow. Regarding the situation of the downstream tip, the trend of the effect of flow velocity is more complex. In case of a low inlet flow velocity of $U_{in}=0.005$ m/s, after a rapid increase, the tip concentration reaches a nearly steady state level which is slightly higher than that in the pure diffusion case. When the inlet velocity increases to 0.015 m/s, the concentration first quickly increases to the value higher than the steady state concentration of $U_{in}=0.005$ m/s. Then it slightly decreases to the end of the simulation. When the imposed inlet velocity is further increased to 0.025 m/s and 0.05 m/s, the concentration ahead of the downstream tip experiences a distinct maximum and then decreases gradually. It is quite evident that the point, where the concentration starts to decrease, indicates the appearance of rotating vortex, while the decreasing rate of concentration is certainly related to the strength of the backflow caused by the vortices.

As analyzed previously, in the solutally driven dendritic growth process, the lower local concentration leads to the higher growth velocity. Therefore, enhanced growth can certainly be expected in the upstream region. As shown in Figs. 10(a) and 10(b), all tip velocities experience an initial rapid growth, and then drop to their steady-state levels. With an increase of the inlet flow velocity from 0.005 m/s to 0.05 m/s, the growth velocity of the upstream tip in the steady-state propagation range is increased by 18% to 89% in comparison with the base case of pure diffusion. On the other hand, as shown in Fig. 10(b), slow inlet flow velocities, such as 0.005 m/s and 0.015 m/s, have almost no influence on the growth of the perpendicular arm. When the flow velocity increases to 0.05 m/s, the vertical tip velocity is found to be about 35% higher than that for without flow. Figure 10(c) illustrates the effect of inlet flow on the growth kinetics of the downstream arm, which is apparently corresponding to the concentration-time history of the downstream tip shown in Fig. 9(c). With an inlet flow velocity of 0.005 m/s, the steady-state growth velocity of the downstream tip decreases about 18% compared to that of no flow case. As the inlet velocity increases, no steady-state growth for the downstream tip has been obtained. Instead, the growth velocity exhibits a minimum and then increases with growth time.
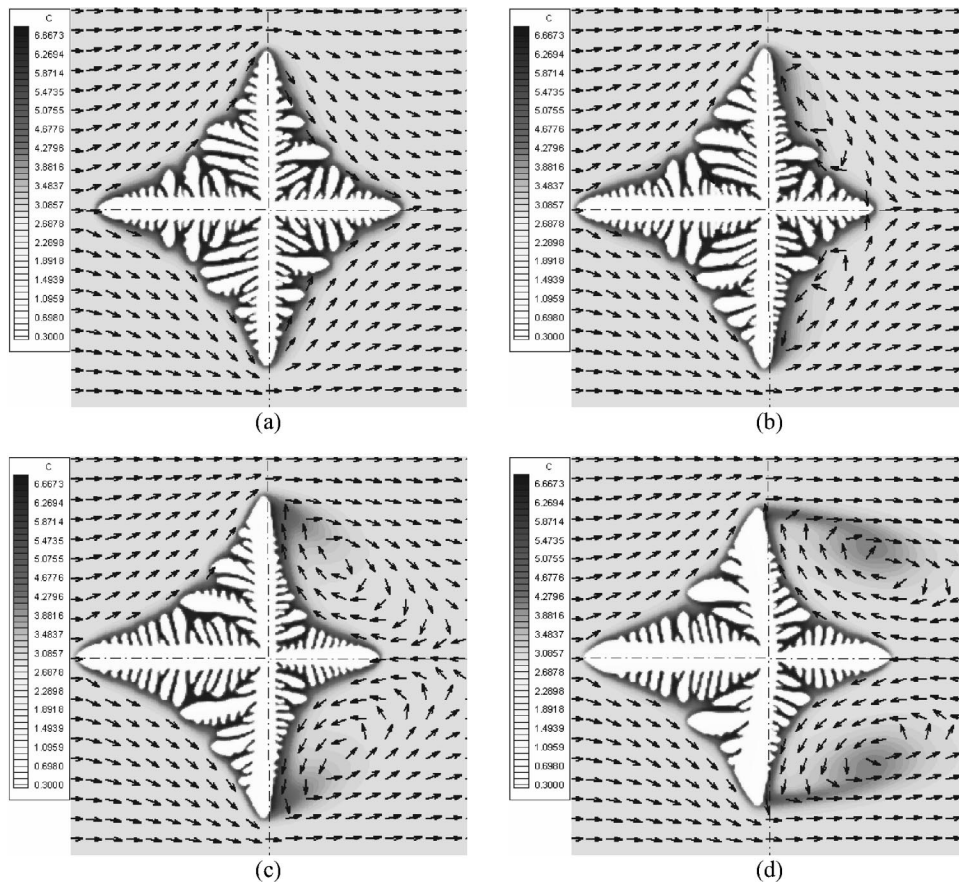
FIG. 8. Simulated dendrite morphologies, solute profiles, and velocity vectors of an Al-3mass%Cu with various inlet flow velocities: (a) $U_{in} = 0.005$ m/s, (b) $U_{in} = 0.015$ m/s, (c) $U_{in} = 0.025$ m/s, and (d) $U_{in} = 0.05$ m/s.

Moreover, the larger the inlet flow velocity, the lower the minimum value. When the inlet flow velocity is 0.05 m/s, the downstream tip reaches a minimum growth velocity of 0.035 in the unit of w_0/τ_0, which is 72% lower than that for pure diffusion. Accordingly, depending upon the direction of fluid flow relative to the direction of tip growth, convection can enforce or retard the dendritic growth compared to the pure diffusion controlled case. Note however, that the times in Figs. 9 and 10 become shorter as the inlet flow velocity increases, whereas the finished solid fraction is all kept the same as shown in Fig. 8. This trend indicates that the overall average velocity of dendritic growth becomes faster as convection gets stronger.

It is worthwhile to mention the computational efficiency of the present model. The calculation times in the present study are about 3 min for simulating a pure diffusive dendritic growth and about 15 min for simulating a convective dendritic growth on a PC Pentium IV with CPU-2.4 GHz, which are much shorter than those of phase-field simulations. For example, Tönhardt and Amberg presented that a phase-field model with an adaptive finite element approach took about 300 CPU hours to calculate a half dendrite growing with convection on a CRAY J932 (1 CPU), and the corresponding case without convection needs about half of this CPU time [7]. Besides, the present model can also be easily extended to 3D, as described in the previous study [47].

V. CONCLUSIONS

The free dendritic growth behavior of an Al-3mass%Cu alloy with melt convection has been studied using a modified cellular automaton model. In the present model, the cellular automaton algorithm is fully coupled with the numerical solution of momentum and species conservation equations. With an excellent computational efficiency, the present model can satisfactorily predict and visualize the complex time-dependent interaction between fluid flow, mass transport in melt, and dendritic growth during solidification. The resulting simulations show that melt convection significantly alters the growth process, producing asymmetrical dendrites with different orientations that all grow faster into the flow and become coarsening in the upstream direction, whereas their growth is largely inhibited in the downstream direction. With an increase of the inlet flow velocity, the tip growth velocity increases in the upstream direction. In addition, the effect of convection is more significant for the upstream tip than the perpendicular tip. On the other hand, as the inlet flow velocity increases, the growth velocity of the downstream tip drops down to the lower level and then increases due to the backflow by the rotating vortices in the downstream region. Although depending upon the direction of fluid flow with respect to the orientation of tip growth, convection can enforce or retard dendritic growth compared to
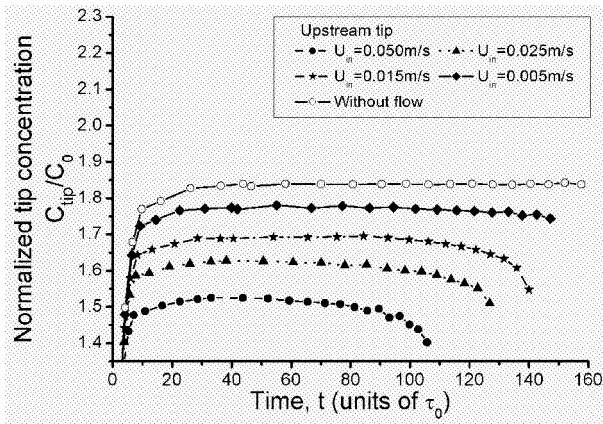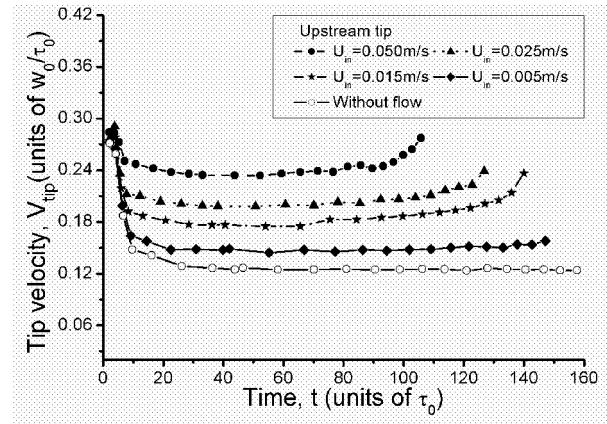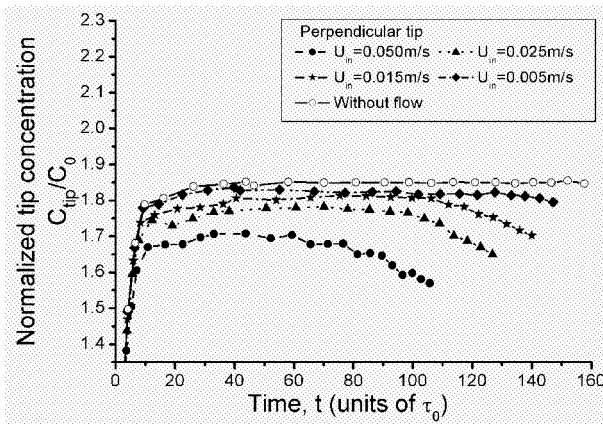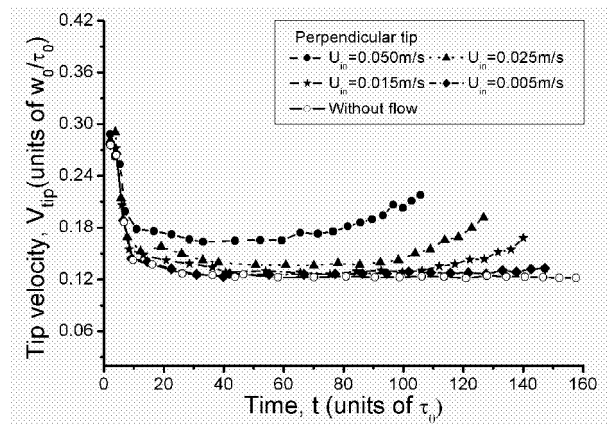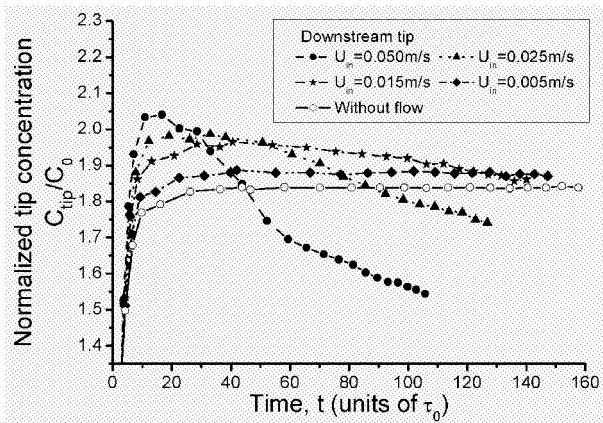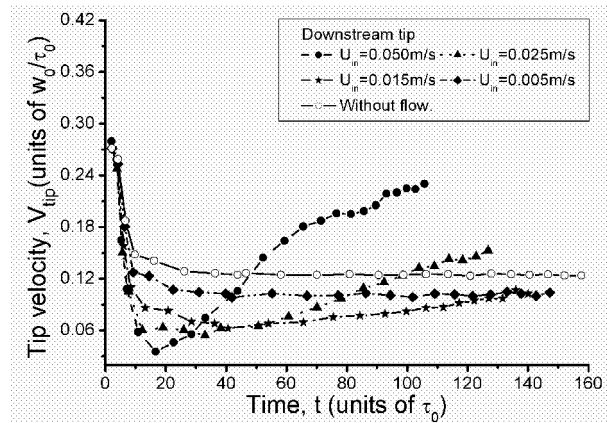
FIG. 9. Effect of inlet flow velocity on the normalized tip concentration: (a) upstream tip, (b) perpendicular tip, and (c) downstream tip.

FIG. 10. Effect of inlet flow velocity on the tip velocity: (a) upstream tip, (b) perpendicular tip, and (c) downstream tip.

the case for the pure diffusion, it accelerates apparently the overall average solidification velocity, since convection efficiently promotes solute transport in the melt. The comparison of present simulation with an experimental observation and a phase-field simulation exhibits the coincident features of asymmetric dendritic growth in the presence of melt convection.

[1] J.C. LaCombe, M.B. Koss, J.E. Frei, C. Giummarra, A.O. Lupulescu, and M.E. Glicksman, Phys. Rev. E **65**, 031604 (2002).

[2] M.E. Glicksman, M.B. Koss, L.T. Bushnell, J.C. Lacombe, and E.A. Winsa, ISIJ Int. **35**, 604 (1995).

[3] X. Tong, C. Beckermann, and A. Karma, Phys. Rev. E **61**, R49 (2000).

[4] J. C. LaCombe, M. B. Koss, A. Lupulescu, L. A. Tennenhouse, and M. E. Glicksman, in *Modeling of Casting, Welding and Advanced Solidification Processes VIII, California, 1998*, edited by B. G. Thomas and C. Beckermann (TMS, Warrendale, PA, 1998), p. 597.

[5] X. Tong, C. Beckermann, A. Karma, and Q. Li, Phys. Rev. E **63**, 061601 (2001).

[6] C. Beckermann, H.-J. Diepers, I. Steinbach, A. Karma, and X. Tong, J. Comput. Phys. **154**, 468 (1999).

[7] R. Tönhardt and G. Amberg, J. Cryst. Growth **213**, 161 (2000).

[8] R. Trivedi, H. Miyahara, P. Mazumder, E. Simsek, and S.N. Tewari, J. Cryst. Growth **222**, 365 (2001).

[9] X. Tong, C. Beckermann, and A. Karma, in *Modeling of Casting, Welding and Advanced Solidification Processes VIII, California, 1998* (Ref. [4]), p. 613.

[10] D.M. Anderson, G.B. McFadden, and A.A. Wheeler, Physica D **151**, 305 (2001).

[11] V. Emsellem and P. Tabeling, J. Cryst. Growth **156**, 285 (1995).

[12] Ph. Bouissou, B. Perrin, and P. Tabeling, Phys. Rev. A **40**, 509 (1989).

[13] D.S. Schraga, J. Cryst. Growth **205**, 410 (1999).

[14] R. Ananth and W.N. Gill, J. Cryst. Growth **179**, 263 (1997).

[15] T. Sawada, K. Takemura, K. Shigematsu, S. Yoda, K. Kawasaki, J. Cryst. Growth **191**, 225 (1998).

[16] Q. Li and C. Beckermann, J. Cryst. Growth **236**, 482 (2002).

[17] V. Emsellem and P. Tabeling, J. Cryst. Growth **166**, 251 (1996).

[18] Y.W. Lee, R. Ananth, and W.N. Gill, J. Cryst. Growth **132**, 226 (1993).

[19] Ph. Bouissou and P. Pelce, Phys. Rev. A **40**, 6673 (1989).

[20] Y.C. Lee and F. Chen, J. Cryst. Growth **154**, 351 (1995).

[21] R.F. Sekerka, S.R. Coriell, and G.B. McFadden, J. Cryst. Growth **154**, 370 (1995).

[22] D.S. Yu and J.J. Xu, J. Cryst. Growth **198/199**, 49 (1999).

[23] J.N. Koster, JOM **49**, 31 (1997).

[24] D.A. Saville and P.J. Beaghton, Phys. Rev. A **37**, 3423 (1988).

[25] L.A. Tennenhous, M.B. Lacombe, J.C. LaCombe, and M.E. Glicksman, J. Cryst. Growth **174**, 82 (1997).

[26] M.B. Koss, J.C. LaCombe, L.A. Tennenhouse, M.E. Glicksman, and E.A. Winsa, Metall. Mater. Trans. A **30A**, 3177 (1999).

[27] N. Al-Rawahi and G. Tryggvason, J. Comput. Phys. **180**, 471 (2002).

[28] P. Lehmann, R. Moreau, D. Camel, and R. Bolcato, J. Cryst. Growth **183**, 690 (1998).

[29] C.W. Lan, C.C. Liu, and C.M. Hsu, J. Comput. Phys. **178**, 464 (2002).

[30] C.W. Lan, C.M. Hsu, C.C. Liu, and Y.C. Chang, Phys. Rev. E **65**, 061601 (2002).

[31] C.W. Lan, C.M. Hsu, and C.C. Liu, J. Cryst. Growth **241**, 379 (2002).

[32] C. Beckermann, Q. Li, and X. Tong, Sci. Technol. Adv. Mater. **2**, 117 (2001).

[33] R. Tönhardt and G. Amberg, Phys. Rev. E **62**, 828 (2000).

[34] R. Tönhardt and G. Amberg, J. Cryst. Growth **194**, 406 (1998).

[35] J.H. Jeong, N. Goldenfeld, and J.A. Dantzig, Phys. Rev. E **64**, 041602 (2001).

[36] D.M. Anderson, G.B. McFadden, and A.A. Wheeler, Physica D **135**, 175 (2000).

[37] J.H. Jeong, J.A. Dantzig, and N. Goldenfeld, Metall. Mater. Trans. A **34A**, 459 (2003).

[38] J.A. Dantzig, J.H. Jeong, and N. Goldenfeld, in *Modeling of Casting, Welding and Advanced Solidification Processes X, Florida, 2003*, edited by D.M. Stefanescu, J. Warren, M. Jolly, and M. Krane (TMS, Warrendale, PA, 2003), p. 13.

[39] H.S. Udaykumar, S. Marella, and S. Krishnan, Int. J. Heat Mass Transfer **46**, 2615 (2003).

[40] D. Juric, in *Modeling of Casting, Welding and Advanced Solidification Processes VIII, California, 1998* (Ref. [4]), p. 605.

[41] G. De Fabritiis, A. Mancini, D. Mansutti, and S. Succi, Int. J. Mod. Phys. C **9**, 1405 (1998).

[42] W. Miller, S. Succi, and D. Mansutti, Phys. Rev. Lett. **86**, 3578 (2001).

[43] Y.H. Shin and C.P. Hong, ISIJ Int. **42**, 359 (2002).

[44] L. Nastac, Acta Mater. **47**, 4253 (1999).

[45] M.F. Zhu and C.P. Hong, ISIJ Int. **41**, 436 (2001).

[46] M.F. Zhu, J.M. Kim, and C.P. Hong, ISIJ Int. **41**, 992 (2001).

[47] M.F. Zhu and C.P. Hong ISIJ Int. **42**, 520 (2002).

[48] C.P. Hong and M.F. Zhu, in *Modeling of Casting, Welding and Advanced Solidification Processes X, Florida, 2003* (Ref. [38]), p. 63.

[49] L. Beltran-Sanchez and D.M. Stefanescu, Metall. Mater. Trans. A **34A**, 367 (2003).

[50] M.F. Zhu and C.P. Hong, Phys. Rev. B **66**, 155428 (2002).

[51] M.F. Zhu, S. Nishido, and C.P. Hong, Int. J. Cast Metals Res. **15**, 273 (2002).

[52] M.F. Zhu and C.P. Hong, in *Modeling of Casting, Welding and Advanced Solidification Processes X, Florida, 2003* (Ref. [38]), p. 91.

[53] A.A. Wheeler, W.J. Boettinger, and G.B. McFadden, Phys. Rev. A **45**, 7424 (1992).

[54] S.G. Kim, W.T. Kim, and T. Suzuki, Phys. Rev. E **60**, 7186 (1999).

[55] R. Trivedi and J.T. Mason, Metall. Trans. **22A**, 235 (1991).

[56] J.J. Xu, J. Cryst. Growth **245**, 134 (2002).

[57] D. Juric and G. Tryggvason, J. Comput. Phys. **123**, 127 (1996).

[58] H.S. Udaykumar, R. Mittal, and W. Shyy, J. Comput. Phys. **153**, 535 (1999).

[59] H. Emmerich, K. Kassner, T. Ihle, and A. Weiss, J. Crystal Growth **211**, 43 (2000).

[60] S. V. Patankar, *Numerical Heat Transfer and Fluid Flow* (Hemisphere Pub. Corp., New York, 1980), p. 126.